

Emergent disorder and sub-ballistic dynamics in quantum simulations of the Ising model using Rydberg atom arrays

Ceren B. Dağ,^{1,2,*} Hanzhen Ma,¹ P. Myles Eugenio,^{3,1} Fang Fang,^{4,1} and Susanne F. Yelin¹

¹*Department of Physics, Harvard University, 17 Oxford Street Cambridge, MA 02138, USA*

²*ITAMP, Harvard-Smithsonian Center for Astrophysics, Cambridge, Massachusetts, 02138, USA*

³*Department of Physics, University of Connecticut, Storrs, CT 06269, USA*

⁴*QuEra Computing Inc., 1284 Soldiers Field Rd, Boston, MA 02135, USA*

Rydberg atom arrays with Van der Waals interactions provide a controllable path to simulate the locally connected transverse-field Ising model (TFIM), a prototypical model in statistical mechanics. Remotely operating the publicly accessible Aquila Rydberg atom array, we experimentally investigate the physics of TFIM far from equilibrium and uncover significant deviations from the theoretical predictions. Rather than the expected ballistic spread of correlations, the Rydberg simulator exhibits a sub-ballistic spread, along with a logarithmic scaling of entanglement entropy in time — all while the system mostly retains its initial magnetization. By modeling the atom motion in tweezer traps, we trace these effects to an emergent natural disorder in Rydberg atom arrays, which we characterize with a minimal random spin model. We further experimentally explore the different dynamical regimes hosted in the system by varying the lattice spacing and the Rabi frequency. Our findings highlight the crucial role of atom motion in the many-body dynamics of Rydberg atom arrays at the TFIM limit, and propose simple benchmark measurements to test for its presence in future experiments.

Unprecedented control of Rydberg atoms in tweezer traps present a unique opportunity to physicists to prepare fundamentally interesting and technologically useful quantum states of matter [1–8]. A particularly intriguing aspect of Rydberg atom arrays interacting with Van der Waals (vdW) interactions is the possibility of realizing the prototypical model of quantum statistical mechanics: the transverse field Ising model (TFIM). Besides exhibiting a quantum phase transition [9], TFIM also has rich behavior when driven out of equilibrium [10–16]. One nonequilibrium behavior of TFIM is the ballistic spread of correlations when it is quenched, which originates from the constant propagation speed of the excitations generated due to the quench [12]. This also leads to a volume-law entangled state with a linearly increasing entanglement entropy in time [17]. Here we report on the experimental observation of instead a sub-ballistic propagation in a one-dimensional Rydberg atom array under a quench [Figure 2(a)], which subsequently generates sub-volume law entangled states with logarithmic increase of entanglement entropy in time against the theoretical prediction. One might think that this behavior could originate from the constrained kinematics due to Rydberg blockade [6]. However at the TFIM limit we are never within the blockade radius, $a/R_b \geq 1$ where $R_b = (C_6/\sqrt{\Omega^2 + \Delta^2})^{1/6}$ [18], which casts the TFIM limit as a different regime of Rydberg atom arrays from the PXP model limit [6]. Our tensor network simulations instead, trace this unexpected phenomenon to *the motion of atoms* that are trapped in tweezers, Fig. 1. Due to finite temperature, $T \sim 15\mu\text{K}$ [18], atom motion gives rise to emergent disorder breaking the Z_2 symmetry in the TFIM in the wake of a sudden quench. We then detect localized and thermal regimes in which the

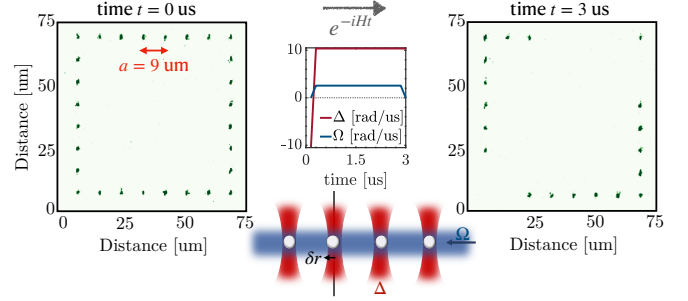


Figure 1. A measurement sequence on Aquila atom array trapped in tweezers with all atoms in the ground state at $t = 0$ evolving to the final state measured at $t = 3\mu\text{s}$. The machine images, provided by QuEra Computing, shows our lattice geometry and the pulse sequence of the experiment where the Rabi frequency Ω and the detuning Δ are suddenly quenched, i.e., ramped in 50ns. Due to thermal fluctuations, atoms move inside the traps which gives rise to a positional uncertainty δr .

initial magnetization is either retained or lost, accompanied by a logarithmic or fast increase in quantum Fisher information (QFI), respectively. Inspired by the experimental data, we introduce a minimal random spin model to describe the physics of the Rydberg atom array when it is mapped to TFIM, which can be utilized in future theoretical studies.

We emphasize the consequences of atom motion having a role in many-body dynamics: Effective Z_2 symmetry breaking in anti-ferromagnetic TFIM prevents the formation of spontaneous ferromagnetism at the top of the spectrum, $|\psi_{\text{FM}}\rangle_{\pm} \propto |\uparrow\uparrow\cdots\uparrow\rangle \pm |\downarrow\downarrow\cdots\downarrow\rangle$. Hence, the prevalent idea of utilizing sudden quenches, instead of slow ramps, to probe spontaneous symmetry breaking

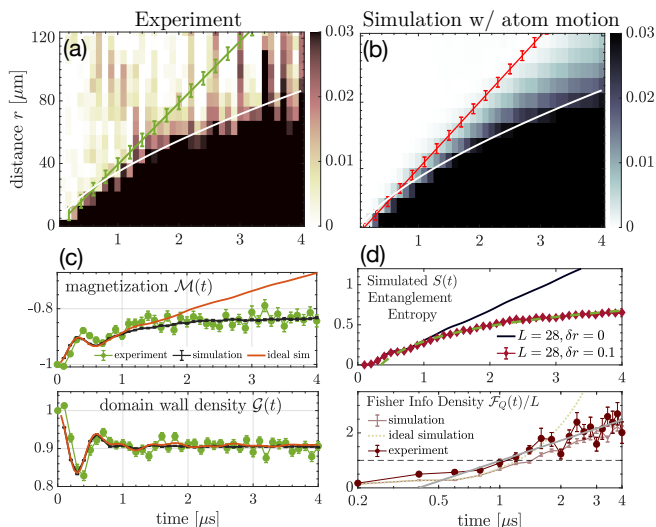


Figure 2. (a) Measured and (b) simulated lightcone of quasi-particles generated following a quench to Rabi frequency $\Omega = 2.2 \text{ rad}/\mu\text{s}$ at the TFIM limit. The lightest quasi-particle velocity substantially decreases due to atom motion following a sub-ballistic lightcone. (c) Measured and simulated magnetization $\mathcal{M}(t)$ and domain-wall density $\mathcal{G}(t)$ compared to the ideal simulation. (d) Upper panel: Simulated bi-partite entanglement entropy $S(t)$ with (red-diamonds) and without (black-solid) atom motion. The green-dashed line is a logarithmic fit showing the sub-volume law character of $S(t)$. Lower panel: Measured and simulated quantum Fisher information density exhibiting also a logarithmic scaling in time (marked with solid-gray), compared to a power-law scaling in the ideal system (dotted-cream). All error bars are standard error of the mean (s.e.m).

(SSB) phase transition in Ising models [13, 14, 19, 20] is actually not attainable in current Rydberg simulators due to significant atom motion in many-body dynamics. Nonetheless, we find a trace of the SSB transition of TFIM in the time-averaged magnetization and domain-wall density, with Z_2 symmetry explicitly broken.

Experimental setup. We remotely operate Aquila Rydberg atom array designed by QuEra Computing [18]. Figure 1 shows the rectangular ring geometry of our setup with $9\mu\text{m}$ distance between 28 atoms, and the quench protocol. Periodic boundary conditions enhance data quality by providing protection against edge effects and enabling faster statistics in many-body physics. The technical details and limitations of the setup can be found in Aquila whitepaper [18]. The Rydberg simulator Hamiltonian can be mapped to the spin-1/2 mixed-field Ising model with vdW interactions [4, 21, 22],

$$\begin{aligned}
 H(t) = & J \sum_r^L \sigma_r^z \sigma_{r+1}^z + \frac{J}{26} \sum_r^L \sigma_r^z \sigma_{r+2}^z \\
 & + \sum_r^L h_x(t) \sigma_r^x - \sum_r^L h_z(t) \sigma_r^z, \quad (1)
 \end{aligned}$$

with periodic boundary conditions and system size L . The interaction strength, transverse and longitudinal fields read

$$J = \frac{C_6}{4a^6}, h_x(t) = \frac{\Omega(t)}{2}, h_z(t) = \frac{1}{2}(\Delta(t) - \Delta_{\text{ising}}), (2)$$

in terms of the experimentally tunable parameters Rabi frequency $\Omega(t)$, detuning $\Delta(t)$, the atom distance a , and the Rydberg interaction coefficient $C_6 = 5.42 \times 10^{-24} \text{ Hz m}^6$. When the detuning is set to $\Delta_{\text{ising}} = 4J(1 + \frac{1}{26})$ — a threshold value that guarantees $h_z(t) = 0$, we achieve the TFIM limit. We start the quench protocol from a polarized state, e.g., $|\downarrow\downarrow \cdots \downarrow\rangle$, i.e., all atoms are in their ground states on a Rydberg simulator at detuning $\Delta = -10.34 \text{ rad}/\mu\text{s}$. Then we quench both detuning and Rabi frequency simultaneously to the TFIM limit, i.e., $\Delta = 10.34 \text{ rad}/\mu\text{s}$ and $\Omega \leq 15.7 \text{ rad}/\mu\text{s}$, in 50ns and hold the system until the measurement time $t \leq 4\mu\text{s}$. We compute the averaged connected equal-time correlators $\mathcal{G}_r^{\text{conn}}(t) = \frac{1}{L} \sum_i G_{i,r}^{\text{conn}}(t)$ where $G_{i,r}^{\text{conn}}(t) = \langle \sigma_i^z(t) \sigma_{i+r}^z(t) \rangle - \langle \sigma_i^z(t) \rangle \langle \sigma_{i+r}^z(t) \rangle$ in order to determine the lightcone dynamics, in addition to the time-evolved magnetization $\mathcal{M}(t) := \frac{1}{L} \sum_i \langle \sigma_i^z(t) \rangle$ and domain-wall density $\mathcal{G}(t) := \frac{1}{L} \sum_i \langle \sigma_i^z(t) \sigma_{i+1}^z(t) \rangle$ to probe the Z_2 symmetry breaking and the dynamical regimes. We compute the fluctuations of normalized total magnetization $\frac{L}{2} \mathcal{M}(t)$ with $\mathcal{F}_Q(t)/L = L \left(\langle \mathcal{M}(t)^2 \rangle - \langle \mathcal{M}(t) \rangle^2 \right)$, which is also the QFI of the generated dynamical pure state in the unitary numerical simulations, and indirectly probes the entanglement [23]. When we compute $\mathcal{F}_Q(t)/L$ for the experimental data, it acts as an upper bound to the actual QFI of the dynamical state [24].

Sub-ballistic spread of correlations and entanglement dynamics. Since the interactions are anti-ferromagnetic in the Rydberg atom array, a quench from $|\downarrow\downarrow \cdots \downarrow\rangle$ excites the many-body system to the high energy states. In ideal conditions, this quench protocol would give rise to a linear lightcone probed by $G_{i,r}^{\text{conn}}$ at any i due to translational invariance as computationally confirmed with time-evolving block decimation (TEBD) algorithm in tensor networks [25], see SM [26]. Consequently the entanglement entropy of the dynamical state increases linearly in time, black-solid in Figure 2(d), a signature of the entangled pairs of quasi-particles generated due to quench [17]. In this dynamical regime, \mathcal{M} exponentially decays to zero in time [12], whereas \mathcal{G} remains larger than 1/2 in long-time limit [14], Figure 2(c) showing that the initial magnetization is eventually lost, and the dynamically generated state always has a finite domain-wall density.

The lightcone $\mathcal{G}_r^{\text{conn}}(t)$ computed with the experimental data in Figure 2(a) after readout-error mitigation [26] demonstrates a sub-ballistic spread of correlations, instead of ballistic, for a quench from polarized state to $h_x/J = 0.43$ (or $\Omega \sim 2.2 \text{ rad}/\mu\text{s}$ at $a = 9\mu\text{m}$).

To determine the origin of this behavior in the many-body dynamics, we simulate the Rydberg atom array Hamiltonian on tensor networks [25] and model the error sources including atom motion, spatial detuning fluctuations, shot-to-shot fluctuations in the detuning and Rabi frequency. Atom motion is modeled with a normal distribution for the uncertainty in the atom positions $\delta r = 0.1\mu\text{m}$ determining the initial positions of atoms, and Maxwell-Boltzmann distribution for the initial velocities determined by the atom temperature $15\mu\text{K}$. The atom positions at later times are deterministically found by solving the equations of motion for each atom independently. See the End Matter for the details on the modeling of other uncertainties. Unless stated otherwise, the simulation results in the plots include all uncertainties. Nevertheless, we find that the dominant mechanism underlying our experimental observations is the atom motion [26]. The tensor network simulation given in Figure 2(b) reproduces the sub-ballistic behavior well, [see [26] for temporal cross-sections with statistical error bars]. Ideally the quasi-particles would exhibit a ballistic lightcone with a maximum speed of $v_c \sim 40\text{m/s}$ which can be analytically determined from $v_c \simeq 2\Omega a$ if $h_x/J < 1$ [12], shown with green and red in Figs. 2(a) and (b), respectively. However, the quantum many-body dynamics slow down under significant atom motion turning the spread of correlations to sub-ballistic, with $r \simeq 34.6t^{0.66}$, from ballistic. This is successfully captured by the numerical modeling in Fig. 2(b) with $r \simeq 34.5t^{0.67}$. Hence, we find that the simple theoretical picture painted above breaks down on a Rydberg simulator due to atom motion. Let us note that other uncertainties do not affect the ballistic behavior of the clean TFIM [26]. For this set of parameters we are right at the blockade radius, which could indeed lead to enhanced thermal fluctuations causing sub-ballistic lightcones. Given a decohering TFIM would give rise to halting spread of correlations over time, $v_c = 0$, sub-ballistic spread is indeed a plausible trend in the intermediate timescales.

Other observables follow suit. The numerically computed entanglement entropy exhibits a sub-volume law behavior with a logarithmic increase in time, Fig. 2(d). Simulated QFI in Fig. 2(d) for unitary dynamics also exhibits a logarithmic increase in time, and importantly it successfully models the experimental $\mathcal{F}_Q(t)$ and its temporal scaling. An array with no atom motion would exhibit a power-law increase of QFI in time, dotted line $\mathcal{F}_Q(t)/L \propto t^{1.6}$. Hence the data demonstrates the role of atom motion in the entanglement of the states generated far from equilibrium. Remembering that the particular $\mathcal{F}_Q(t)$ we study here is a cumulative effect of all possible spatial correlations in the z -basis, the logarithmic scaling is consistent with the sub-ballistic lightcone in Fig. 2(a). Furthermore, the magnetization decays to a finite value, Fig. 2(c) implying that the many-body system partially retains its initial condition. The domain-wall

density does not significantly differ from the ideal case. This is because $\mathcal{G}(t)$ cannot differentiate between explicit and spontaneous symmetry breaking.

Minimal random spin model. Inspired by these experimental observations and to gain more insight about the role of atom motion in many-body dynamics, we write a minimal yet realistic many-body model for the TFIM limit of the Rydberg atom arrays. This time-independent model incorporates only the effect of atom motion into the Hamiltonian with the uncertainty in the atom positions δr ,

$$H^{\text{eff}} = \sum_r J_r \sigma_r^z \sigma_{r+1}^z + \frac{\Omega}{2} \sum_r \sigma_r^x - \sum_r h_r \sigma_r^z, \quad (3)$$

$$J_r = \mathcal{N}\left(\frac{1}{4} \frac{C_6}{a^6}, \frac{3}{2} \frac{C_6 \delta r}{a^7}\right), h_r = \mathcal{N}\left(0, 3 \frac{C_6 \delta r}{a^7}\right), \quad (4)$$

where $\mathcal{N}(\mu_N, \sigma_N)$ stand for normal distribution with mean μ_N and standard deviation σ_N . We observe that the atom motion effectively introduces random disorder to the Hamiltonian $\mathcal{W} \equiv \sigma_N(h_r)/\mu_N(J_r) \sim 12\delta r/a$. Here $\sigma_N(h_r)$ and $\mu_N(J_r)$ stand for the standard deviation of h_r and the mean of J_r . Although such disorder is always present in Rydberg simulators, its effect is suppressed and likely becomes insignificant in many-body dynamics away from the TFIM limit where $\mu_N(h_r) \gg \sigma_N(h_r)$ holds.

To probe the dependence of disorder \mathcal{W} on the lattice spacing a , we quench to $\Omega \sim 11.7 \text{ rad}/\mu\text{s}$ at the TFIM limit and vary only the lattice constant between $a = 6 - 10.5\mu\text{m}$ with the ratio $a/R_b = 1 - 1.21$ when a increases. Fig. 3(a) panels show the QFI for select lattice constants. We spot a large difference between experiment and ideal simulations due to atom motion, except at $a = 10.5\mu\text{m}$, (a₄). At large atom distances, QFI slowly increases to its maximum value with a good match between simulations in the presence and absence of atom motion. This suggests that the system approaches its clean limit $W \sim 0$, as the lattice constant increases, $h_x/J \gg 1$. At $a = 7\mu\text{m}$, (a₁), the temporal scaling of QFI is consistent with a logarithmic scaling surpassing $\mathcal{F}_Q/L = 1$, and hence suggesting many-body localization-like behavior [23, 27, 28]. Consistently, the initial magnetization is mostly retained in the experiment, Fig. 3(b₁). In contrast, at $a = 8\mu\text{m}$ in (a₂), QFI quickly increases to its maximum value in $0.2\mu\text{s}$ and remains constant after both in numerics and experiment, while the initial magnetization quickly decays to zero, (b₂). Hence, we bear witness to localized and extended regimes in the quench dynamics of Rydberg atom arrays due to atom motion.

In full simulations in Fig. 3, we keep the positional uncertainty fixed at $\delta r = 0.1\mu\text{m}$, as this is experimentally expected based on atom motion. However we find for some lattice constants, even the full simulation does not reproduce the experiment, e.g., at $a = 7.5\mu\text{m}$ in (a₃).

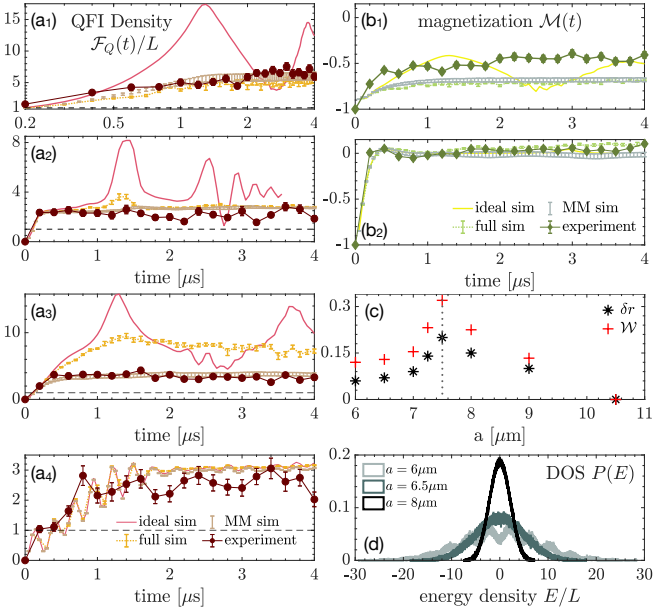


Figure 3. Naturally disordered quantum many-body system following a quench to $\Omega = 11.7$ rad/ μs at the TFIM limit numerically and experimentally probed with (a) QFI and (b) magnetization for different lattice constants. Panels (a): (a₁), (a₂), (a₃) and (a₄) respectively plot the QFI for $a = 7\mu\text{m}$, $a = 8\mu\text{m}$, $a = 7.5\mu\text{m}$ and $a = 10.5\mu\text{m}$. Panels (b): (b₁) and (b₂) respectively plot the magnetization for $a = 7\mu\text{m}$ and $a = 8\mu\text{m}$. For both (a) and (b), the legends include the experiment, simulations with and without uncertainties, utilizing the minimal model (MM) in Eq. (3). (c) The positional uncertainty δr for different lattice constants in the MM and the resulting disorder strength \mathcal{W} . (d) Density of states in MM for an open-boundary chain of size $L = 14$ at lattice constants $a = 6, 6.5, 8\mu\text{m}$. All error bars are s.e.m. Error bars for the MM simulations are due to 10 different statistically similar systems with different configurations of J_r and h_r .

This is a signature of physics laying beyond the capability of current unitary simulations, e.g., decoherence [29]. In order to phenomenologically capture such effects by the minimal model, we treat δr in Eq. (3) as a fitting parameter. Hence, we determine a set of phenomenological δr by fitting the magnetization fluctuations \mathcal{F}_Q/L of Eq. (3) to those of experimental data at a fixed Rabi frequency, given \mathcal{F}_Q/L is more susceptible to the changes in δr . Consequently, we find that δr changes with lattice constant, and maximizes at $a \sim 7.5\mu\text{m}$, Fig. 3(c). Therefore, the disorder parameter \mathcal{W} of the minimal model exhibits a nontrivial dependence on the lattice constant. It is not a coincidence that where δr and \mathcal{W} peak is also where the full simulation fails the most. Our lack of knowledge about the experimental time evolution contributes to the disorder of the unitary minimal model.

We diagonalize Eq. (3) with determined \mathcal{W} for $L = 14$, and examine the spectral statistics of the minimal model by averaging over the ratio of consecutive energy gaps $\langle r \rangle = \langle \min[E_{n+1} - E_n, E_n - E_{n-1}] / \max[E_{n+1} -$

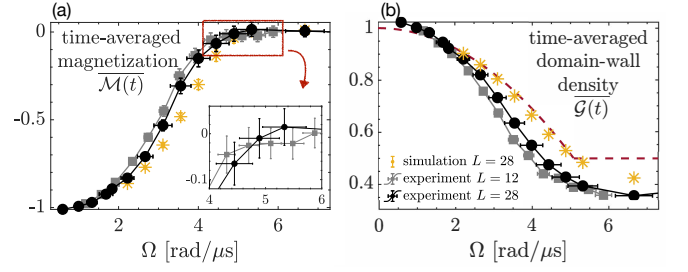


Figure 4. Time-averaged (a) magnetization and (b) domain-wall density to experimentally probe a trace of Z_2 symmetry breaking of spontaneous symmetry breaking transition at the clean TFIM. Experiments are performed with quenches to different Rabi frequencies Ω and hence transverse field h_x at the TFIM limit at fixed lattice constant $a = 9\mu\text{m}$. Orange-stars are the simulated results with all uncertainties included. Inset in (a) zooms on the crossover region. (b) also shows the ideal TFIM results in the infinite time limit with red-dashed line. All error bars are s.e.m.

$E_n, E_n - E_{n-1}]_n$ where E_n is the n^{th} eigenenergy [30]. The minimal model exhibits chaotic spectrum with $\langle r \rangle = 0.53$ at $a = 8\mu\text{m}$, and nearly integrable spectrum with $\langle r \rangle = 0.408$ at $a = 6.5\mu\text{m}$. We numerically observe in Fig. 3(d) that the density of states of Eq. (3) peaks as we increase the lattice constant, while the mini-bands appear at $a = 6\mu\text{m}$.

Trace of SSB transition. Ferromagnetic TFIM with vdW interactions, $h_z = 0$, hosts an SSB transition between an SSB ferromagnet and a paramagnet at $h_{\text{qcp}} = 1.027J$. Meanwhile $\mathcal{G}(t)$ in the thermodynamic limit and infinite time exhibits a discontinuity at the SSB transition of ferromagnetic TFIM signalling the transition in the wake of a quench [14]. The same physics holds in the anti-ferromagnetic TFIM: Following a quench from a polarized state to any h_x , time-averaged magnetization is $|\overline{\mathcal{M}(t \rightarrow \infty)}| = 0$. Whereas $\overline{\mathcal{G}(t \rightarrow \infty)} > 1/2$ and $\overline{\mathcal{G}(t \rightarrow \infty)} = 1/2$ for a quench to $h_x < h_{\text{qcp}}$ and $h_x \geq h_{\text{qcp}}$, respectively, as depicted with red-dashed lines in Fig. 4(b).

The disorder already breaks the Z_2 symmetry, leading to finite magnetization in time when we quench to $h_x < h_{\text{qcp}}$, as in Fig. 2(d), instead of an exponential decay to zero [12]. We use this signature to define an order parameter-like quantity based on the time-average of experimental magnetization $|\overline{\mathcal{M}(t)}|$ and domain-wall density $\overline{\mathcal{G}(t)}$ between $[0, 4]\mu\text{s}$, and plot these values in Figure 4 with respect to Rabi frequency for two different system sizes, $L = 28$ and $L = 12$, at fixed $a = 9\mu\text{m}$, and hence at a fixed $\mathcal{W} \sim 0.13$. The magnetization exhibits an experimental crossover at $\Omega_c \sim 5$ rad/ μs (with corresponding crossover transverse-field $h_c \sim J$) between two system sizes where $|\overline{\mathcal{M}(t)}| > 0$ is observed for $h_x < h_c$, and $|\overline{\mathcal{M}(t)}| \sim 0$ for $h_x \geq h_c$, see inset in Fig. 4(a). $|\overline{\mathcal{M}(t)}|$ tends to increase (decrease) with increasing system size in $h_x < h_c$ ($h_x > h_c$) with $h_c \sim h_{\text{qcp}}$. The crossover trend

of $|\overline{\mathcal{M}(t)}|$ is absent without the atom motion, even when the time-averaging is performed in the experimental time interval $[0, 4]\mu\text{s}$ [26]. Meanwhile, the domain-wall density reaches its minimum around h_c with a value $\overline{\mathcal{G}(t)} \sim 0.4$, which undershoots $\frac{1}{2}$ due to explicit Z_2 symmetry breaking. These results show that it is possible to take on a trace of Z_2 SSB transition in an experimental data of a disordered many-body system pushed out of equilibrium.

Conclusions and Outlook. Our work experimentally demonstrates the remarkable effect of atom motion in quantum many-body dynamics on a Rydberg simulator, and provides a minimal model that captures these observations. This model can be used to predict the many-body dynamics of Rydberg atom arrays under a protocol that quenches the system to its TFIM limit. While different disordered Ising models are present in the literature [31–33], Hamiltonian Eq. (3) is yet to be fully explored in theory. Importantly, can introducing decoherence to the minimal model modify the predicted random disorder profile with respect to atom distance? If decoherence is responsible for the mismatch between full simulation and experiment around $a = 7.5\mu\text{m}$, why chains with different lattice spacings decohere differently, and whether the effect of decoherence is maximized due to a nonequilibrium criticality [29] are interesting questions to answer in the future.

TFIM limit is rather a fine-tuned point on a Rydberg atom array, which explains the importance of atom motion in many-body dynamics at this limit. Our results imply more generally the fine-tuned points in other platforms [34–36], can be susceptible to particle motion. While we exclusively discussed ferromagnetic initial states due to simplicity, the atom motion also dominates for quenches from Neel states, and possibly for slow ramps, to the low energy sector of the Ising Hamiltonian. This suggests that more advanced cooling techniques are needed to faithfully realize Ising models with only transverse field on Rydberg simulators. Alternatively, it is an interesting question to ask whether one can synchronize the atoms in tweezers [37] to combat the emergent disorder. Our work sets simple benchmarking experiments far from equilibrium with spatio-temporal spread of correlations, quantum Fisher information, magnetization and domain-wall density to test whether the atom motion is sufficiently suppressed in quantum many-body dynamics.

Acknowledgments. Authors thank A. Bylinskii, M. Kojncica, T. Macrì, C. W. Wächtler, N. Yao and M. D. Lukin for stimulating discussions, Amazon Web Services for the Cloud Credit for Research Program credits granted towards utilizing Aquila in this project, and QuEra Computing for technical assistance on Aquila, Majd Hamdan and P. Lopes for the machine images in Figure 2. C.B.D was supported with the ITAMP grant No. 2116679. SFY acknowledges support from the NSF through grant PHY-2207972 and the Q-Ideas HDR (OAC-2118310).

End Matter. Here we explain in detail the data collection and processing on Aquila. We calibrate our measurements before any many-body measurement by doing a two-photon resonance experiment on a collection of independent atoms on 2D geometry. In this experiment, we suddenly quench the Rabi frequency from 0 to the desired Rabi frequency, Ω , keep the detuning constant at a value Δ and make a measurement at time $t_\pi = \pi/\Omega$. We repeat the same measurement for different detuning values, and obtain the experimental excitation probability with respect to detuning. The excitation probability can be analytically derived via quantum optics techniques [38],

$$P_e(\Delta) = \frac{\Omega^2}{\Omega^2 + \Delta^2} \sin^2 \left(\sqrt{\Omega^2 + \Delta^2} \frac{t_\pi}{2} \right).$$

We fit our experimental data to $P_e(\Delta)$ to find the systematic global detuning shift and the calibrated Rabi frequency. All reported values in the Letter are calibrated values. We then correct for the systematic detuning shift in all many-body measurements done in the same day. Let us emphasize the importance of the calibration experiment before many-body measurements at the TFIM limit. Since TFIM limit is a fine-tuned point in detuning, it is crucial to correct for this systematic uncertainty rather than modeling it in numerics.

Calibration experiment also provides us $1-\sigma$ deviation from the measured values. We apply bootstrap technique [39] to first observe the emergence of normal distribution for calibrated Rabi frequency and detuning, and then to extract $1-\sigma$ deviation. The latter is used in numerical modeling of Rabi frequency and detuning fluctuations from shot-to-shot. We also locally apply bootstrap technique to each atom to determine the spatial detuning profile across the many-body chain, and find that this is roughly sinusoidal across the array [26]. Based on this method, we find negligible differences in the Rabi frequency of the atoms, and hence we do not include spatial variations in Rabi frequency in our numerical modeling.

We apply error mitigation to the many-body data with confusion matrices derived for one- and two-body observables incorporating the readout errors [26, 40]. In addition to that, we postselect the final bit strings based on the correct initial state, which is the state where all atoms are in their ground state. Occasionally the machine starts from a wrong initial state, or pre-sequence imaging has errors. We omit final bit strings from such experiments.

* ceren.dag@harvard.edu

[1] A. Omran, H. Levine, A. Keesling, G. Semeghini, T. T. Wang, S. Ebadi, H. Bernien, A. S. Zibrov, H. Pichler, S. Choi, J. Cui, M. Rossignolo, P. Rembold, S. Montangero, T. Calarco, M. Endres, M. Greiner, V. Vuletić, and M. D. Lukin, *Science* **365**, 570 (2019).

- [2] S. de Léséleuc, V. Lienhard, P. Scholl, D. Barredo, S. Weber, N. Lang, H. P. Büchler, T. Lahaye, and A. Browaeys, *Science* **365**, 775 (2019).
- [3] A. Keesling, A. Omran, H. Levine, H. Bernien, H. Pichler, S. Choi, R. Samajdar, S. Schwartz, P. Silvi, S. Sachdev, *et al.*, *Nature* **568**, 207 (2019).
- [4] A. Browaeys and T. Lahaye, *Nature Physics* **16**, 132 (2020).
- [5] P. Scholl, M. Schuler, H. J. Williams, A. A. Eberharter, D. Barredo, K.-N. Schymik, V. Lienhard, L.-P. Henry, T. C. Lang, T. Lahaye, *et al.*, *Nature* **595**, 233 (2021).
- [6] S. Ebadi, T. T. Wang, H. Levine, A. Keesling, G. Semeghini, A. Omran, D. Bluvstein, R. Samajdar, H. Pichler, W. W. Ho, *et al.*, *Nature* **595**, 227 (2021).
- [7] H. Bernien, S. Schwartz, A. Keesling, H. Levine, A. Omran, H. Pichler, S. Choi, A. S. Zibrov, M. Endres, M. Greiner, *et al.*, *Nature* **551**, 579 (2017).
- [8] G. Semeghini, H. Levine, A. Keesling, S. Ebadi, T. T. Wang, D. Bluvstein, R. Verresen, H. Pichler, M. Kalinowski, R. Samajdar, *et al.*, *Science* **374**, 1242 (2021).
- [9] S. Sachdev, *Quantum Phase Transitions* (Cambridge University Press, 2001).
- [10] K. Sengupta, S. Powell, and S. Sachdev, *Phys. Rev. A* **69**, 053616 (2004).
- [11] P. Calabrese, F. H. L. Essler, and M. Fagotti, *Phys. Rev. Lett.* **106**, 227203 (2011).
- [12] P. Calabrese, F. H. L. Essler, and M. Fagotti, *Journal of Statistical Mechanics: Theory and Experiment* **2012**, P07016 (2012).
- [13] M. Heyl, F. Pollmann, and B. Dóra, *Phys. Rev. Lett.* **121**, 016801 (2018).
- [14] P. Titum, J. T. Iosue, J. R. Garrison, A. V. Gorshkov, and Z.-X. Gong, *Phys. Rev. Lett.* **123**, 115701 (2019).
- [15] C. B. Dağ and K. Sun, *Phys. Rev. B* **103**, 214402 (2021).
- [16] C. B. Dağ, Y. Wang, P. Uhrich, X. Na, and J. C. Halimeh, *Phys. Rev. B* **107**, L121113 (2023).
- [17] P. Calabrese and J. Cardy, *Journal of Statistical Mechanics: Theory and Experiment* **2005**, P04010 (2005).
- [18] J. Wurtz, A. Bylinskii, B. Braverman, J. Amato-Grill, S. H. Cantu, F. Huber, A. Lukin, F. Liu, P. Weinberg, J. Long, S.-T. Wang, N. Gemelke, and A. Keesling, “Aquila: Quera’s 256-qubit neutral-atom quantum computer,” (2023), [arXiv:2306.11727 \[quant-ph\]](https://arxiv.org/abs/2306.11727).
- [19] E. Nicklas, M. Karl, M. Höfer, A. Johnson, W. Muesel, H. Strobel, J. Tomkovič, T. Gasenzer, and M. K. Oberthaler, *Phys. Rev. Lett.* **115**, 245301 (2015).
- [20] C. B. Dağ, P. Uhrich, Y. Wang, I. P. McCulloch, and J. C. Halimeh, *Phys. Rev. B* **107**, 094432 (2023).
- [21] H. Kim, Y. Park, K. Kim, H.-S. Sim, and J. Ahn, *Phys. Rev. Lett.* **120**, 180502 (2018).
- [22] H. Labuhn, D. Barredo, S. Ravets, S. De Léséleuc, T. Macrì, T. Lahaye, and A. Browaeys, *Nature* **534**, 667 (2016).
- [23] J. Smith, A. Lee, P. Richerme, B. Neyenhuis, P. W. Hess, P. Hauke, M. Heyl, D. A. Huse, and C. Monroe, *Nature Physics* **12**, 907–911 (2016).
- [24] S. L. Braunstein and C. M. Caves, *Phys. Rev. Lett.* **72**, 3439 (1994).
- [25] ITensor Library (version 2.0.11) <http://itensor.org>.
- [26] See Supplementary Material.
- [27] D. M. Basko, I. L. Aleiner, and B. L. Altshuler, *Annals of Physics* **321**, 1126 (2006), [arXiv:cond-mat/0506617 \[cond-mat.mes-hall\]](https://arxiv.org/abs/cond-mat/0506617).
- [28] R. Nandkishore and D. A. Huse, *Annual Review of Condensed Matter Physics* **6**, 15–38 (2015).
- [29] F. Fang, K. Wang, V. S. Liu, Y. Wang, R. Cimmino, J. Wei, M. Bintz, A. Parr, J. Kemp, K.-K. Ni, and N. Y. Yao, “Probing critical phenomena in open quantum systems using atom arrays,” (2024), [arXiv:2402.15376 \[quant-ph\]](https://arxiv.org/abs/2402.15376).
- [30] V. Oganesyan and D. A. Huse, *Phys. Rev. B* **75**, 155111 (2007).
- [31] D. A. Huse, R. Nandkishore, V. Oganesyan, A. Pal, and S. L. Sondhi, *Phys. Rev. B* **88**, 014206 (2013).
- [32] J. A. Kjäll, J. H. Bardarson, and F. Pollmann, *Phys. Rev. Lett.* **113**, 107204 (2014).
- [33] D. Trapin, J. C. Halimeh, and M. Heyl, *Phys. Rev. B* **104**, 115159 (2021).
- [34] C. Monroe, W. C. Campbell, L.-M. Duan, Z.-X. Gong, A. V. Gorshkov, P. W. Hess, R. Islam, K. Kim, N. M. Linke, G. Pagano, P. Richerme, C. Senko, and N. Y. Yao, *Rev. Mod. Phys.* **93**, 025001 (2021).
- [35] P. Richerme, Z.-X. Gong, A. Lee, C. Senko, J. Smith, M. Foss-Feig, S. Michalakakis, A. V. Gorshkov, and C. Monroe, *Nature* **511**, 198 (2014).
- [36] S.-A. Guo, Y.-K. Wu, J. Ye, L. Zhang, W.-Q. Lian, R. Yao, Y. Wang, R.-Y. Yan, Y.-J. Yi, Y.-L. Xu, *et al.*, *Nature*, 1 (2024).
- [37] M. Samoylova, N. Piovella, G. R. Robb, R. Bachelard, and P. W. Courteille, *Optics express* **23**, 14823 (2015).
- [38] P. Meystre and M. Sargent, *Elements of quantum optics* (Springer Science & Business Media, 2007).
- [39] “Resampling techniques,” in *Statistical Analysis Techniques in Particle Physics* (John Wiley and Sons, Ltd) Chap. 4, pp. 63–87.
- [40] S. Bravyi, S. Sheldon, A. Kandala, D. C. McKay, and J. M. Gambetta, *Phys. Rev. A* **103**, 042605 (2021).

Supplementary Material: Emergent disorder and sub-ballistic dynamics in quantum simulations of the Ising model using Rydberg atom arrays

Ceren B. Dağ, Hanzhen Ma, P. Myles Eugenio, Fang Fang, Susanne F. Yelin

I. TEMPORAL CROSS-SECTIONS ON LIGHT CONE

In most of the many-body experiments, we collect 200 bit strings at each time. Due to post-selection based on the correct initial state, the number of useful bit strings reduces to around ~ 160 with a high enough post-selection rate. Hence the sampling number affects the standard error of the mean (s.e.m). The typical s.e.m. in the light cone figures is on the order of ~ 0.03 , see Figs. S1. This is the reason why we set the colorbar in the light cone figures to 0.03, which is our experimental resolution. The numerical modeling match the experimental data well within the error bars.

II. SPATIAL DETUNING FLUCTUATIONS

As already explained in End Matter, we find the spatial profile of the detuning fluctuations via bootstrapping each atom individually. We do not find significant changes of this profile over multiple experiments performed over a period of 4 months. Figure S2 shows this profile over the many-body chain of 28 atoms with $9 \mu\text{m}$ distance between each atom. This profile can be approximated to be periodic, and hence acts like a shallow superlattice potential on the atoms. Our full numerical simulations take this spatial detuning profile into account.

III. DETAILS OF THE NUMERICAL MODELING ON TENSOR NETWORKS

We consider atom motion, spatial detuning profile, shot-to-shot fluctuations in the detuning and Rabi frequency in our numerical modeling. When atom motion is not considered in tensor network simulations, the sub-ballistic behavior in the light cones and the saturation of the magnetization over time observed in the experiment cannot be explained. Fig. S3 shows the experimental data against the numerical modeling without atom motion. Let us note that the shot-to-shot fluctuations are modeled by normal distribution. Hence it is reasonable to expect their effect on the final results, averaged over many bit strings, to be negligible, which is what we also observe in numerics [not shown]. Spatial detuning profile has a non-negligible effect, and indeed exhibits a slowing down of the magnetization decay, however we still do not observe a saturation as visible in experimental data. More importantly, the light cone without atom motion does not exhibit a sub-ballistic spread of correlations. Rather the propagation of correlations is still ballistic with a renormalized speed, $v'_c = 29.1 \text{ m/s}$. This is straightforward to understand as the spatial detuning profile simply imprints a superlattice potential on the emergent quasi-particles of the many-body system, modifying the correlation speeds rather than the nature of it.

IV. QFI AT DIFFERENT LATTICE SPACINGS

Here we share the entire set of QFI data for lattice spacings $a = 6, 6.5, 7, 7.5, 8, 10.5 \mu\text{m}$ in Fig. S4 where the full simulation also uses the fitted positional uncertainty δr , different from the simulation results discussed in the main text. Here we choose to utilize the fitted positional uncertainty in the full simulation to show the match between full and minimal model simulations when δr is fixed to the same value. Hence the minimal model is a good approximation to the Rydberg Hamiltonian at the TFIM limit in the presence of the atom motion when all parameters are taken to be the same.

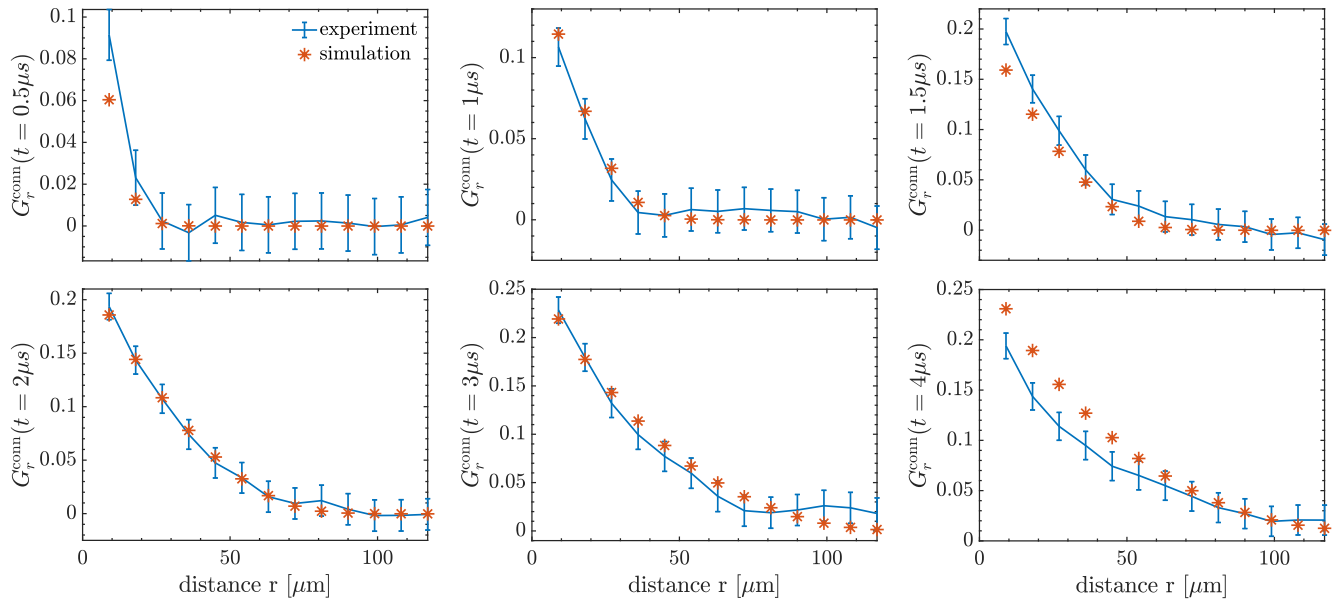


Figure S1. Temporal cross-sections of $\mathcal{G}_r^{\text{conn}}(t)$ at different times between $t = 0.5\mu\text{s}$ and $t = 4\mu\text{s}$ for the light cone plotted in main text, Figure 2(a). Experiment (solid-blue) and simulation with atom motion (orange-stars) match well.

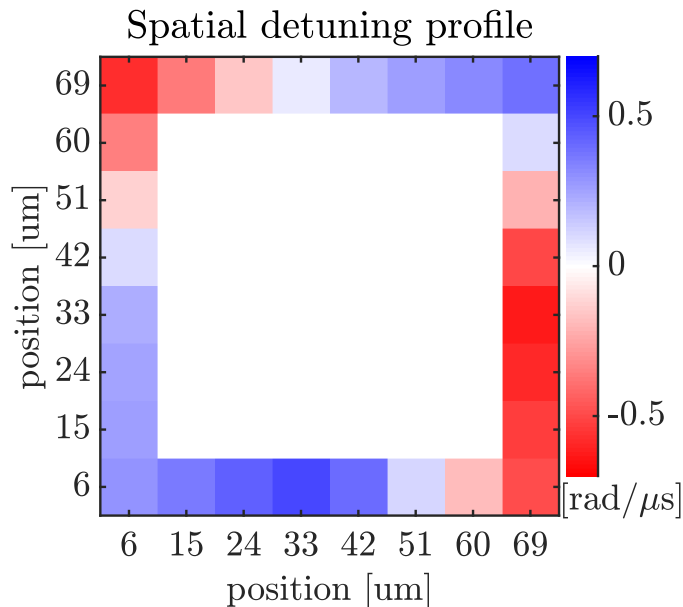


Figure S2. Spatial detuning profile on a 28 atom periodic chain. The profile is roughly periodic across the chain, and should be considered as a long-wavelength fluctuation of the detuning on the set global detuning value.

V. IDEAL TIME-AVERAGED OBSERVABLES IN EXPERIMENTAL TIME INTERVAL

Here we share the simulations of time-averaged magnetization and domain-wall density averaged between $[0, 4]\mu\text{s}$ omitting the atom motion, hence in ideal conditions, Figure S5. The tensor network simulations are still performed for the Rydberg atom array, and they take into account the next-nearest neighbor interactions. Note that these observables in the clean TFIM exhibit strong finite-size effects in their time evolution as revivals, as already seen in Figure 3(b₁) in the main text. Hence, the time average over $[0, 4]\mu\text{s}$ actually also averages over such finite-size effects.

Specifically we observe the tendency of magnetization to smoothen around the critical point, $\Omega \sim 5 \text{ rad}/\mu\text{s}$ as the

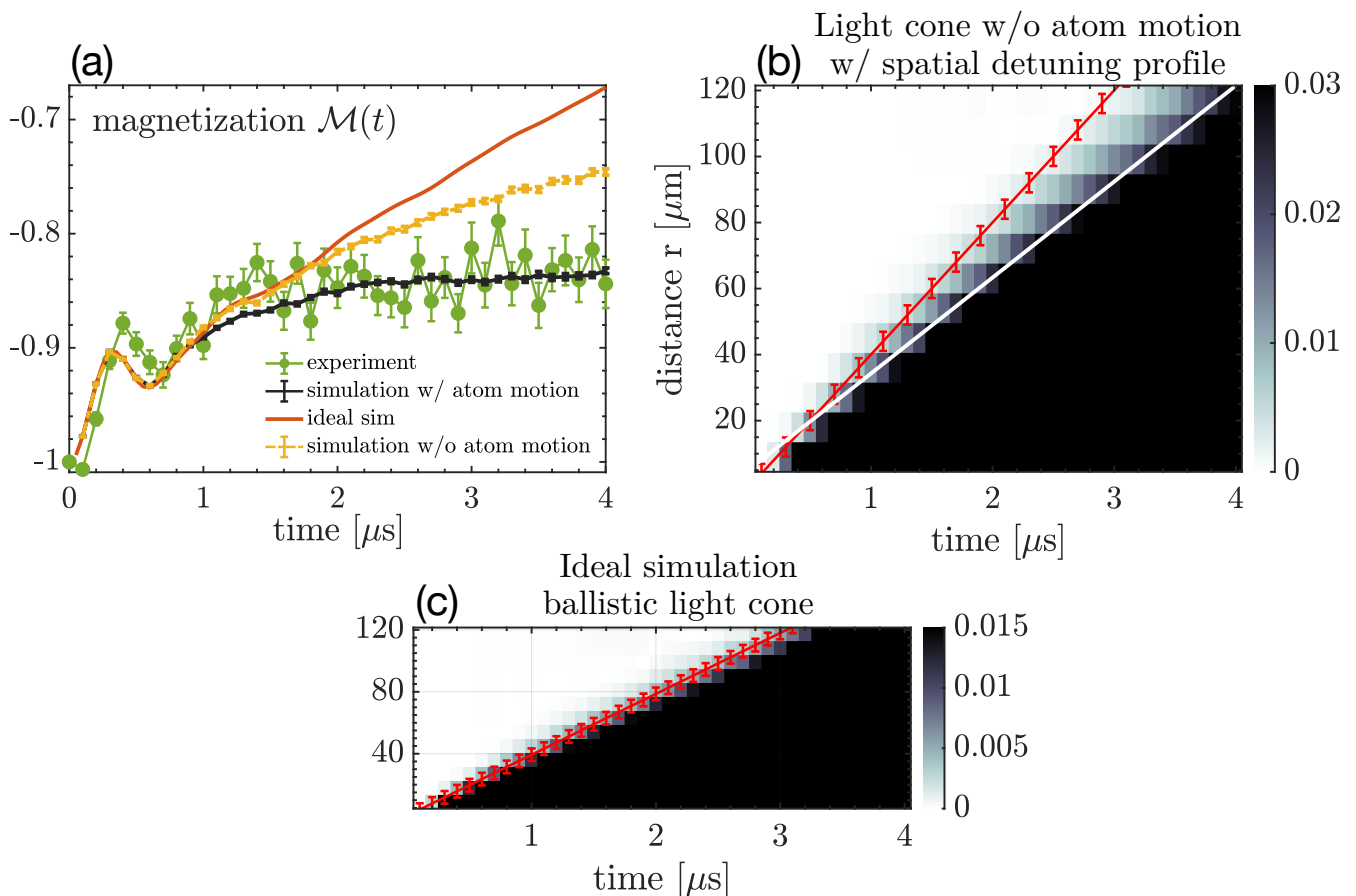


Figure S3. Numerical modeling without atom motion. (a) Magnetization with atom motion is black as in Letter, without atom motion, but with spatial detuning profile, is depicted with orange, cannot capture the saturation in later times. (b) Light cone without atom motion but with spatial detuning profile does not exhibit a sub-ballistic behavior, rather the ballistic propagation continues with a renormalized correlation speed (white-solid). (c) Ideal simulation exhibits the theoretically expected ballistic light cone.

system size increases, in contrast to the experimental data (see main text) and the full simulation with atom motion (yellow-stars), which sharpen around the critical point. This is expected, as the infinite-time and thermodynamic limit response in ideal conditions is featureless, the pink-dotted line in (a). Hence, we observe once more the important role of atom motion in modeling the experiment and capturing the correct physical interpretation behind the experimental data. Fig. S5(b) shows the tendency of the domain-wall density to sharpen around the critical point as the system size increases in the ideal conditions. This is a reason why this quantity was proposed to probe the quantum critical point of TFIM in the first place [14]. However as already shown in the Letter, Figure 3, the longitudinal field generated by the atom motion at the TFIM limit causes the domain-wall density to undershoot $\overline{\mathcal{G}}(t) = 1/2$. Experimental data also looks smoother compared to the data in ideal conditions, which we attribute to the presence of significant atom motion.

VI. EMPLOYED ERROR MITIGATION TECHNIQUE

Perhaps the most important uncertainty in the Aquila Rydberg atom simulator is the readout errors of the final bit strings. Let us define $p_{i \rightarrow j}$ as the probability of state $|i\rangle$ to be measured as state $|j\rangle$ where $i, j = 0, 1$. Naturally, $p_{i \rightarrow i} + p_{i \rightarrow j} = 1$ for $j \neq i$. For Aquila, $p_{0 \rightarrow 1} = 0.01$ and $p_{1 \rightarrow 0} = 0.05$.

A confusion matrix \mathcal{C} encodes all readout errors. For example, \mathcal{C} for one-site measurements follows as,

$$\mathcal{C} = \begin{pmatrix} p_{0 \rightarrow 0} & p_{1 \rightarrow 0} \\ p_{0 \rightarrow 1} & p_{1 \rightarrow 1} \end{pmatrix}. \quad (\text{S1})$$

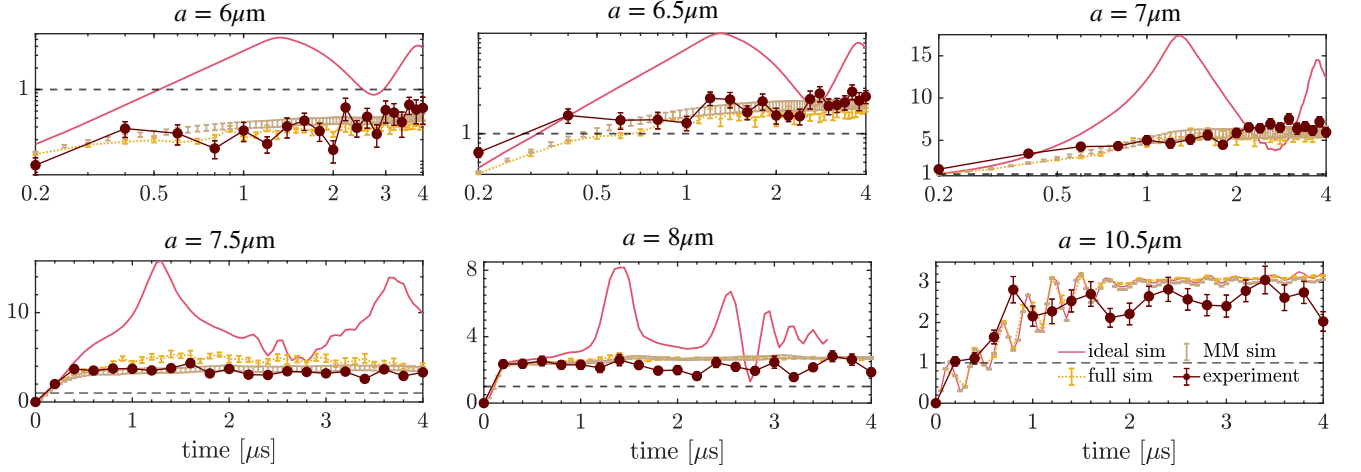


Figure S4. Quantum Fisher information for lattice spacings $a = 6, 6.5, 7, 7.5, 8, 10.5 \mu\text{m}$ showing the experiment data, ideal simulation, MM simulation and the full simulation both with the fitted positional uncertainty. Hence the full simulation results differ from the ones presented in Figure 3 in the main text, as they are not fixed to $\delta r = 0.1 \mu\text{m}$.

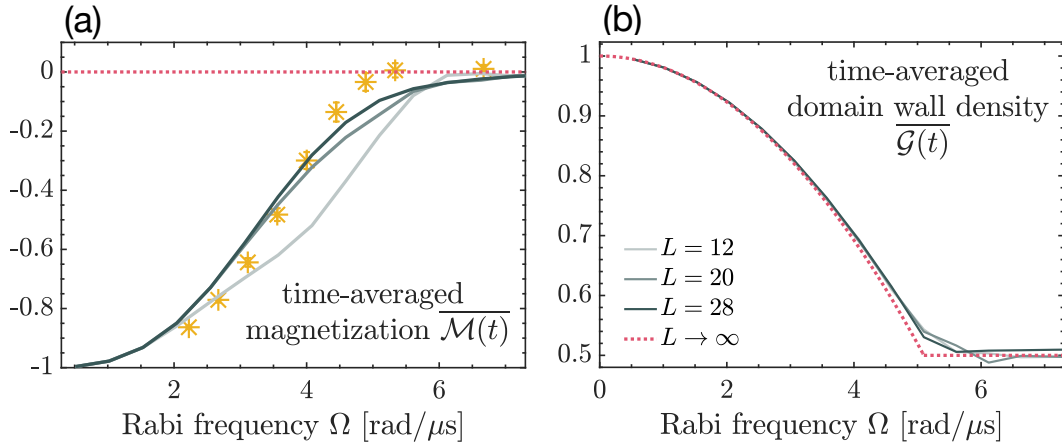


Figure S5. The time-averaged (a) magnetization and (b) domain wall density in ideal conditions for three different system sizes $L = 12, 20, 28$. The pink dotted line shows the results in the thermodynamic limit and at infinite time. Subfigure (a) includes the full simulation with uncertainties at $L = 28$ for comparison.

Assuming the one-site measurement is in Z basis, the error-mitigated expectation value of single-site magnetization $\langle \tilde{\sigma}_i^z \rangle$ at any time and site will be,

$$\langle \tilde{\sigma}_i^z \rangle = \frac{1}{N} \sum_{k=1}^N \left(-\langle 0 | \mathcal{C}^{-1} | s_k \rangle + \langle 1 | \mathcal{C}^{-1} | s_k \rangle \right), \quad (\text{S2})$$

where $|0\rangle = (1, 0)^T$ and $|1\rangle = (0, 1)^T$, and $|s_k\rangle$ denotes either of two states that was measured in the experiment in the k^{th} shot. Summation over k is the statistical average over N many shots.

We also measure two-site observables such as $\langle \sigma_z^i(t) \sigma_z^j(t) \rangle$. Confusion matrix for such observables are written as,

$$\mathcal{C} = \begin{pmatrix} p_{00 \rightarrow 00} & p_{01 \rightarrow 00} & p_{10 \rightarrow 00} & p_{11 \rightarrow 00} \\ p_{00 \rightarrow 01} & p_{01 \rightarrow 01} & p_{10 \rightarrow 01} & p_{11 \rightarrow 01} \\ p_{00 \rightarrow 10} & p_{01 \rightarrow 10} & p_{10 \rightarrow 10} & p_{11 \rightarrow 10} \\ p_{00 \rightarrow 11} & p_{01 \rightarrow 11} & p_{10 \rightarrow 11} & p_{11 \rightarrow 11} \end{pmatrix}, \quad (\text{S3})$$

where the following holds with $p_{ij \rightarrow kl}$ denoting two qubit readout error probabilities,

$$\begin{aligned} p_{00 \rightarrow 01} &= p_{00 \rightarrow 10} = p_{0 \rightarrow 1}(1 - p_{0 \rightarrow 1}), & p_{00 \rightarrow 11} &= p_{0 \rightarrow 1}^2, & p_{00 \rightarrow 00} &= (1 - p_{0 \rightarrow 1})^2, \\ p_{11 \rightarrow 01} &= p_{11 \rightarrow 10} = p_{1 \rightarrow 0}(1 - p_{1 \rightarrow 0}), & p_{11 \rightarrow 00} &= p_{1 \rightarrow 0}^2, & p_{11 \rightarrow 11} &= (1 - p_{1 \rightarrow 0})^2, \\ p_{01 \rightarrow 01} &= (1 - p_{0 \rightarrow 1})(1 - p_{1 \rightarrow 0}), & p_{01 \rightarrow 00} &= (1 - p_{0 \rightarrow 1})p_{1 \rightarrow 0}, & p_{01 \rightarrow 11} &= p_{0 \rightarrow 1}(1 - p_{1 \rightarrow 0}), \\ p_{01 \rightarrow 10} &= p_{0 \rightarrow 1}p_{1 \rightarrow 0}, & p_{10 \rightarrow 10} &= (1 - p_{1 \rightarrow 0})(1 - p_{0 \rightarrow 1}), & p_{10 \rightarrow 11} &= (1 - p_{1 \rightarrow 0})p_{0 \rightarrow 1}, \\ p_{10 \rightarrow 00} &= p_{1 \rightarrow 0}(1 - p_{0 \rightarrow 1}), & p_{10 \rightarrow 01} &= p_{1 \rightarrow 0}p_{0 \rightarrow 1}. \end{aligned}$$

This leads to the error-mitigated two-point correlator $\langle \widetilde{\sigma_z^i \sigma_z^j} \rangle$

$$\langle \widetilde{\sigma_z^i \sigma_z^j} \rangle = \frac{1}{N} \sum_{k=1}^N \left(\langle 00| + \langle 11| - \langle 01| - \langle 10| \right) \mathcal{C}^{-1} |s_k s'_k \rangle.$$

While these can be numerically calculated for each many-body bit string, due to the simplicity of the confusion matrix we can write analytical formulae for magnetization \mathcal{M} and nearest-neighbor two-point correlator \mathcal{G} . Consider a general n -qubit state

$$|\psi\rangle = \sum_{m=1}^{2^n} A_m |S_m\rangle \quad (\text{S4})$$

where $|S_m\rangle$ are 2^n basis states. Each of the states corresponds to a bit string such as $|0110\dots10\rangle$. Let

$$|S_m\rangle = |s_1^{(m)}\rangle |s_2^{(m)}\rangle \dots |s_k^{(m)}\rangle \dots |s_n^{(m)}\rangle. \quad (\text{S5})$$

The error-free magnetization $\widetilde{\mathcal{M}}$ is

$$\widetilde{\mathcal{M}} = \frac{1}{n} \sum_{k=1}^n \langle \sigma_k^z \rangle = \frac{1}{n} \sum_{k=1}^n \sum_{m=1}^{2^n} |A_m|^2 \langle S_m | \sigma_k^z | S_m \rangle = \frac{1}{n} \sum_{k=1}^n \sum_{m=1}^{2^n} |A_m|^2 \langle s_k^{(m)} | \sigma_k^z | s_k^{(m)} \rangle \quad (\text{S6})$$

with

$$\langle s_k^{(m)} | \sigma_k^z | s_k^{(m)} \rangle = \begin{cases} +1 & , |s_k^{(m)}\rangle = |1\rangle \\ -1 & , |s_k^{(m)}\rangle = |0\rangle \end{cases} \quad (\text{S7})$$

For any site k , there is a probability $p_{i \rightarrow j}$ to replace $\langle i | \sigma_k^z | i \rangle$ by $\langle j | \sigma_k^z | j \rangle$. The magnetization with readout errors is then

$$\begin{aligned} \mathcal{M} &= \frac{1}{n} \sum_{k=1}^n \left\{ \sum_{m \in \{m' | s_k^{(m')} = 1\}} |A_m|^2 \langle s_k^{(m)} | \sigma_k^z | s_k^{(m)} \rangle + \sum_{m \in \{m' | s_k^{(m')} = 0\}} |A_m|^2 \langle s_k^{(m)} | \sigma_k^z | s_k^{(m)} \rangle \right\} \quad (\text{S8}) \\ &= \frac{1}{n} \sum_{k=1}^n \left\{ \sum_{m \in \{m' | s_k^{(m')} = 1\}} |A_m|^2 \left[p_{1 \rightarrow 1}(+1) + p_{1 \rightarrow 0}(-1) \right] + \sum_{m \in \{m' | s_k^{(m')} = 0\}} |A_m|^2 \left[p_{0 \rightarrow 0}(-1) + p_{0 \rightarrow 1}(+1) \right] \right\} \\ &= \frac{1}{n} \sum_{k=1}^n \left\{ a_k (p_{1 \rightarrow 1} - p_{1 \rightarrow 0}) + b_k (p_{0 \rightarrow 1} - p_{0 \rightarrow 0}) \right\} \end{aligned}$$

where we have defined $a_k = \sum_{m \in \{m' | s_k^{(m')} = 1\}} |A_m|^2$ and $b_k = \sum_{m \in \{m' | s_k^{(m')} = 0\}} |A_m|^2$, with $a_k + b_k = 1$. Using these quantities, the error-free magnetization can be written as

$$\widetilde{\mathcal{M}} = \frac{1}{n} \sum_{k=1}^n (a_k - b_k) \quad (\text{S9})$$

Defining $a = \frac{1}{n} \sum_{k=1}^n a_k$ and $b = \frac{1}{n} \sum_{k=1}^n b_k$, we obtain the following set of equations

$$\begin{aligned} \widetilde{\mathcal{M}} &= a - b \\ \mathcal{M} &= a(p_{1 \rightarrow 1} - p_{1 \rightarrow 0}) + b(p_{0 \rightarrow 1} - p_{0 \rightarrow 0}) \\ 1 &= a + b \end{aligned} \quad (\text{S10})$$

Therefore,

$$\widetilde{\mathcal{M}} = 2 \frac{\mathcal{M} + p_{0 \rightarrow 0} - p_{0 \rightarrow 1}}{p_{1 \rightarrow 1} - p_{1 \rightarrow 0} - p_{0 \rightarrow 1} + p_{0 \rightarrow 0}} - 1. \quad (\text{S11})$$

Aquila has $p_{0 \rightarrow 0} = 0.99$, $p_{0 \rightarrow 1} = 0.01$, $p_{1 \rightarrow 0} = 0.05$ and $p_{1 \rightarrow 1} = 0.95$. For the error-free nearest-neighbor two-point correlator

$$\begin{aligned} \widetilde{\mathcal{G}} &= \frac{1}{n} \sum_{k=1}^n \langle \sigma_k^z \sigma_{k+1}^z \rangle = \frac{1}{n} \sum_{k=1}^n \sum_{m=1}^{2^n} |A_m|^2 \langle s_k^{(m)} s_{k+1}^{(m)} | \sigma_k^z \sigma_{k+1}^z | s_k^{(m)} s_{k+1}^{(m)} \rangle \\ &= \frac{1}{n} \sum_{k=1}^n (c_k - d_k - e_k + f_k) \\ &= c - d - e + f \end{aligned} \quad (\text{S12})$$

where we have defined

$$\begin{aligned} c_k &= \sum_{m \in \{m' | s_k^{(m')} = 0, s_{k+1}^{(m')} = 0\}} |A_m|^2, & d_k &= \sum_{m \in \{m' | s_k^{(m')} = 0, s_{k+1}^{(m')} = 1\}} |A_m|^2 \\ e_k &= \sum_{m \in \{m' | s_k^{(m')} = 1, s_{k+1}^{(m')} = 0\}} |A_m|^2, & f_k &= \sum_{m \in \{m' | s_k^{(m')} = 1, s_{k+1}^{(m')} = 1\}} |A_m|^2 \end{aligned}$$

and $c = \frac{1}{n} \sum_{k=1}^n c_k$, $d = \frac{1}{n} \sum_{k=1}^n d_k$, $e = \frac{1}{n} \sum_{k=1}^n e_k$, $f = \frac{1}{n} \sum_{k=1}^n f_k$. The two-point correlator with the readout errors is

$$\begin{aligned} \mathcal{G} &= c \left[p_{00 \rightarrow 00} (+1) + p_{00 \rightarrow 01} (-1) + p_{00 \rightarrow 10} (-1) + p_{00 \rightarrow 11} (+1) \right] \\ &+ d \left[p_{01 \rightarrow 00} (+1) + p_{01 \rightarrow 01} (-1) + p_{01 \rightarrow 10} (-1) + p_{01 \rightarrow 11} (+1) \right] \\ &+ e \left[p_{10 \rightarrow 00} (+1) + p_{10 \rightarrow 01} (-1) + p_{10 \rightarrow 10} (-1) + p_{10 \rightarrow 11} (+1) \right] \\ &+ f \left[p_{11 \rightarrow 00} (+1) + p_{11 \rightarrow 01} (-1) + p_{11 \rightarrow 10} (-1) + p_{11 \rightarrow 11} (+1) \right] \equiv cx + dy + ez + fw. \end{aligned} \quad (\text{S13})$$

Notice that $y = z$. One can also express the error-free magnetization from these quantities

$$\widetilde{\mathcal{M}} = \frac{1}{2} (2f - 2c + 0 \cdot d + 0 \cdot e) = f - c \quad (\text{S14})$$

leading to the following set of equations

$$\begin{aligned} \widetilde{\mathcal{G}} &= c - d - e + f \\ \mathcal{G} &= cx + dy + ey + fw \\ \widetilde{\mathcal{M}} &= f - c \\ 1 &= c + d + e + f \end{aligned} \quad (\text{S15})$$

Therefore,

$$\widetilde{\mathcal{G}} = - \frac{w + x + 2y + 2(w - x)\widetilde{\mathcal{M}} - 4\mathcal{G}}{w + x - 2y}. \quad (\text{S16})$$